Numerical Investigations on Temperature Distribution and Evolution of Cavitation Bubble Collapsed Near Solid Wall

Minglei Shan[1]*, Yu Yang[1,2], Xuefen Kan[1], Fangyong Shu[1] and Qingbang Han[1]

[1]Jiangsu Key Laboratory of Power Transmission and Distribution Equipment Technology, Hohai University, Changzhou, China, [2]College of Computer and Information, Hohai University, Nanjing, China

The internal temperature distribution and evolution in cavitation bubble can be investigated numerically by a thermal lattice Boltzmann method. The simulation results are consistent with the calculational results of the Rayleigh-Plesset equation and the temperature equation when the cavitation bubble collapses in an infinite liquid medium and satisfy Laplace's law. In this work, a cavitation bubble collapsing near a solid wall is explored to investigate the characteristics and effects of the bubble temperature. The progress of the bubble temperature can be clearly captured from a two-dimensional temperature field. The results show that the bubble temperature can reach extremely high values during both its first and its second collapse. The change of the bubble temperature is highly related to the jet velocity and the liquid pressure. Furthermore, the effects on the bubble temperature of the offset parameters, the initial driving pressure and the initial bubble radius are also studied. The present findings are meaningful for the research of thermodynamics of cavitation.

Keywords: bubble temperature, collapse, lattice Boltzmann method, cavitation, solid wall

INTRODUCTION

Cavitation is usually associated with a decrease in the operational efficiency of device, surface destruction of bodies operating under cavitation conditions (Chahine and Hsiao, 2015). However, the current research on cavitation has achieved the transformation from cavitation damage to rational utilization. For example, cavitation cleaning technology is used to clean the surface of cracks, ultrasonic cleaning technology of glasses, and the use of cavitation bubbles as a transport tool for drugs to deliver drugs to the surface of diseased tissue (Ohl et al., 2006; Verhaagen and Fernández Rivas, 2016; Meullemiestre et al., 2017). The main mechanism of cavitation damage was generally considered to be the effect of micro jets and shock waves (Brennen, 2005; Mason, 2016). In addition to the mechanical mechanism, the thermal effect produced by cavitation is also important in causing material cavitation damage because of the high temperature achieved when the bubble collapses (Suslick et al., 2011; Yusof et al., 2016).

However, there is no definite conclusion about the internal temperature of the bubble because the high temperature in the process of rapid collapse is local and transient. Nowotny (Nowotny, 1942) and Gavranek et al. (Gavranek et al., 1960) observed that the high temperature of the bubble in the final stage of collapse will reduce the strength of metal and can melt a metal surface. Also, because of the fluid medium, the rates of heating and cooling can be more than 1100 K/s (Suslick and Flannigan,

2008), making it difficult to directly measure bubble temperature. Many efforts, both calculations and experiments, have been devoted to investigating the bubble temperature and its effects (Tomita and Shima, 1986; Wang et al., 2001; Cervone et al., 2005; Fujikawa et al., 2006; Dular and Coutier-Delgosha, 2013). However, the cavitation bubble temperatures obtained by theory and by experiment are quite different, so it is not yet possible to from a definite conclusion. In addition, experiments still have not revealed the internal mechanism of the temperature change and distribution in a bubble, numerical simulation methods have become a powerful way to better understand.

The lattice Boltzmann method (LBM), a mesoscopic numerical approach, has been applied to complex multiphase flow fields (Gonnella et al., 2007; Dong et al., 2009; Safari et al., 2010; Gan et al., 2015). The LBM is easy to implement and parallelize, and has clear physical background and high computational efficiency. As one of them, the pseudopotential Shan-Chen (SC) lattice Boltzmann (LB) model has been widely used by the LB community. The most remarkable feature of the SC LB model approach is that the phase separation automatically without interface tracking or interface capturing via an interparticle potential. The first thermal LBM based on the SC model may be credited to Zhang and Chen (Zhang and Chen, 2003). Later, Házi and Márkus (Házi and Márkus, 2008; Márkus and Házi, 2011), Biferale et al. (Biferale et al., 2012; Biferale et al., 2013), and Gong et al. (Gong and Cheng, 2012; Liu and Cheng, 2013) also proposed thermal LB models. The common feature of these models is to solve the thermal LB equation with temperature distribution function to restore the Navier-Stokes-level macroscopic temperature equation. The target temperature equation is a convection-diffusion equation including the source term. Then, based on the above studies, Li et al. (Li et al., 2017) revised the existing thermal model to eliminate the discrete effect of the source term in the target temperature equation, and proposed an improved thermal multi-relaxation-time (MRT) LB model at the same time.

Based on this, Shan et al. (Shan et al., 2016; Shan et al., 2017; Yang et al., 2020; Yang et al., 2021) adopted the above-mentioned thermal MRT LBM to simulate the collapse of the cavitation bubble near the solid wall. The temperature change and dynamic behavior of the bubble were well captured. Previous studies focused on the stage after the cavitation bubble collapsed, but did not deeply analyze the characteristics and effects of the time-dependent bubble temperature. However, both driving pressure and bubble radius affect the temperature in the bubble. An increase of the equilibrium bubble radius will gradually reduce the temperature in the bubble, while an increase of the driving pressure will gradually increase its temperature (Flannigan and Suslick, 2005; Huai et al., 2011). Therefore, the mechanism and effect of the bubble temperature deserve further study.

In this work, an improved thermal MRT LBM is used to investigate cavitation bubble temperature evolution when cavitation bubble collapses near a wall. The basic numerical model is formulated in *Section Numerical Model*. The validation of Laplace's law and the Rayleigh-Plesst equation are described in *Section Model Validation*. Numerical simulations of the bubble collapse near solid wall are

presented in *Section Numerical Results*, which also includes further analysis and discussion. Finally, *Section Conclusion* gives brief conclusions.

NUMERICAL MODEL

The fluid field can be described by density distribution functions. Based on MRT collision operator, the extended LB equation of the density distribution function with external force term can be given as (He et al., 1999; Lallemand and Luo, 2000)

$$f_\alpha(\mathbf{x} + \mathbf{e}_\alpha \delta_t, t + \delta_t) = f_\alpha(\mathbf{x}, t) - \mathbf{M}^{-1} \Lambda \mathbf{M} \big(f_\beta(\mathbf{x}, t) - f_\beta^{eq}(\mathbf{x}, t) \big) + \delta_t S_\alpha', \quad (1)$$

where $f_\alpha(\mathbf{x}, t)$ is the density distribution function at particle position $\mathbf{x}$ and time t, δ_t is the time step and is usually equal to the unit space δ_t. α indicates the number of discrete velocities, and S_α' denotes the forcing term in velocity space. For the D2Q9 lattice model, the orthogonal transformation matrix $\mathbf{M}$ is shown as (Mohamad, 2017)

$$\mathbf{M} = c \begin{bmatrix} 1 & 1 & 1 & 1 & 1 & 1 & 1 & 1 & 1 \\ -4 & -1 & -1 & -1 & -1 & 2 & 2 & 2 & 2 \\ 4 & -2 & -2 & -2 & -2 & 1 & 1 & 1 & 1 \\ 0 & 1 & 0 & -1 & 0 & 1 & -1 & -1 & 1 \\ 0 & -2 & 0 & 2 & 0 & 1 & -1 & -1 & 1 \\ 0 & 0 & 1 & 0 & -1 & 1 & 1 & -1 & -1 \\ 0 & 0 & -2 & 0 & 2 & 1 & 1 & -1 & -1 \\ 0 & 1 & -1 & 1 & -1 & 0 & 0 & 0 & 0 \\ 0 & 0 & 0 & 0 & 0 & 1 & -1 & 1 & -1 \end{bmatrix}, \quad (2)$$

where c is the lattice constant, which equal to $\delta_x / \delta_t = 1$, and the diagonal matrix

$$\Lambda = diag\big(\tau_\rho^{-1}, \tau_e^{-1}, \tau_\varsigma^{-1}, \tau_j^{-1}, \tau_q^{-1}, \tau_j^{-1}, \tau_q^{-1}, \tau_v^{-1}, \tau_v^{-1} \big), \quad (3)$$

where $\tau_\rho^{-1} = \tau_v^{-1} = \tau_j^{-1} = 1.0$, $\tau_\varsigma^{-1} = \tau_e^{-1} = 0.8$, $\tau_q^{-1} = 1.1$. In the momentum space, the density distribution function $\mathbf{m} = \mathbf{M} f$ and the equilibrium density distribution $\mathbf{m}^{eq} = \mathbf{M} f^{eq}$, which can be expressed as

$$\mathbf{m} = \mathbf{M} f = M_{\alpha\beta} f_\beta = \big(\rho, e, \varsigma, j_x, q_x, j_y, q_y, p_{xx}, p_{xy} \big)^T, \quad (4)$$

$$\mathbf{m}^{eq} = \mathbf{M} f^{eq} = M_{\alpha\beta} f_\beta^{eq} = \big(\rho, e^{eq}, \varsigma^{eq}, j_x, q_x^{eq}, j_y, q_y^{eq}, p_{xx}^{eq}, p_{xy}^{eq} \big)^T$$
$$= \rho \big(1, -2 + 3|\mathbf{v}|^2, 1 - 3|\mathbf{v}|^2, v_x, -v_x, v_y, -v_y, v_x^2 - v_y^2, v_x v_y \big)^T. \quad (5)$$

where $\rho = \sum_\alpha f_\alpha$ is the macroscopic density. $\mathbf{v}$ represents the macroscopic velocity and $|\mathbf{v}| = v_x^2 + v_y^2$.

The collision process of momentum space can be transformed from **Eq. 1** into

$$\mathbf{m}^* = \mathbf{m} - \Lambda(\mathbf{m} - \mathbf{m}^{eq}) + \delta_t \Big(I - \frac{\Lambda}{2} \Big) S, \quad (6)$$

where $\mathbf{m}^* = (m_0^*, m_1^*, \ldots, m_8^*)$, $S = \mathbf{M} S'$ is the forcing term, in which $S' = (S_0', S_1', \cdots, S_8')^T$, and I is the unit tensor.

The Streaming Process is Shown as

$$f_\alpha (\boldsymbol{x} + \boldsymbol{e}_\alpha \delta_t, t + \delta_t) = f_\alpha^* (\boldsymbol{x}, t), \tag{7}$$

where $f^* = \boldsymbol{M}^{-1} \boldsymbol{m}^*$. The macroscopic velocity of the **Eq. 5** can be calculated by

$$\rho \boldsymbol{v} = \sum_\alpha \boldsymbol{e}_\alpha f_\alpha + \frac{\delta_t}{2} F, \tag{8}$$

where the fluid-fluid interactive force is $F = (F_x, F_y)$ in 2D space, which is given by (Shan, 2006; Shan, 2008)

$$F(\boldsymbol{x}) = -G\psi(\mathbf{x}) \sum_{\alpha=1}^N \omega (|\boldsymbol{e}_\alpha|^2) \psi (\mathbf{x} + \boldsymbol{e}_\alpha) \boldsymbol{e}_\alpha, \tag{9}$$

where $\omega (|\vec{e}_\alpha|^2)$ denotes the weight coefficient with $\omega(1) = 1/3$ and $\omega(2) = 1/12$, G represents the strength of interaction between fluids. $\psi(x)$ is the interaction potential, which is given by (Sbragaglia et al., 2007)

$$\psi(x) = \sqrt{2 (p_{EOS} - \rho c_s^2)/Gc^2}, \tag{10}$$

where $c_S = c/\sqrt{3}$ is the lattice sound speed, p_{EOS} is a prescribed non-ideal equation of state (EOS), coupling the Peng-Robinson (P-R) EOS, which is given by (Yuan and Schaefer, 2006)

$$p_{EOS} = \frac{\rho \delta T}{1 - b\rho} - \frac{a\vartheta(T)\rho^2}{1 + 2b\rho - b^2\rho^2}, \tag{11}$$

where $a = 0.45724 R^2 T_c^2/p_c$, $b = 0.0778 R T_c/p_c$, and δ is the gas constant.
$\vartheta(T) = [1 + (0.37464 + 1.54226\omega - 0.26992\omega^2) (1 - \sqrt{\frac{T}{T_c}})]^2$, in which $\omega = 0.344$ is the acentric factor, T_c and p_c indicate the critical temperature and pressure. The constants $a = 2/49$, $b = 2/21$ and $\delta = 1$ are used in the present study (He et al., 1998).

For the D2Q9 lattice, Li *et al.*'s (Li et al., 2012; Li et al., 2013) forcing scheme can be given by

$$S = \begin{bmatrix} 0 \\ 6(v_x F_x + v_y F_y) + \dfrac{0.75\varepsilon |F|^2}{\psi^2 \delta_t (\tau_e - 0.5)} \\ -6(v_x F_x + v_y F_y) - \dfrac{0.75\varepsilon |F|^2}{\psi^2 \delta_t (\tau_\varsigma - 0.5)} \\ F_x \\ -F_x \\ F_y \\ -F_y \\ 2(v_x F_x - v_y F_y) \\ (v_x F_y + v_y F_x) \end{bmatrix}. \tag{12}$$

The adjustable coefficient ε, seen in **Eq. 12**, which can make the mechanical stability solution and the thermodynamic consistency requirement approximately the same in a wide temperature range.

Now turns to solving the temperature equation, the target temperature equation is written as (Guo et al., 2002; Li et al., 2016)

$$\frac{\partial T}{\partial t} + \nabla \cdot (\boldsymbol{v}T) = \nabla \cdot (\alpha \nabla T) + \phi, \tag{13}$$

where the thermal diffusivity is $\alpha = \frac{k}{\rho c_v}$, k indicates the thermal conductivity, ρ denotes the macroscopic density and c_v is the specific heat at constant volume. The source term ϕ can be written as

$$\phi = T \left[1 - \frac{1}{\rho c_v} \left(\frac{\partial p_{EOS}}{\partial T} \right)_\rho \right] \nabla \cdot \boldsymbol{v}. \tag{14}$$

The discrete equation of temperature distribution function can be given by

$$g_\alpha (\boldsymbol{x} + \boldsymbol{e}_\alpha \delta_t, t + \delta_t) - g_\alpha (\boldsymbol{x}, t) = -\bar{\Lambda}_{\alpha\beta} (g_\beta - g_\beta^{eq}) \big|_{(\boldsymbol{x}.t)} + \delta_t Q_\alpha^{'} (\boldsymbol{x}, t), \tag{15}$$

where $g_\alpha (x, t)$ is the temperature distribution function at position x and time t, $Q_\alpha^{'}$ represents the source term of the discrete velocity space, and $\bar{\Lambda}_{\alpha\beta} = (\boldsymbol{M}^{-1} \boldsymbol{\Lambda} \boldsymbol{M})_{\alpha\beta}$ is the collision matrix.

Eq. 15 can be converted as follows

$$\boldsymbol{n}^* = \boldsymbol{n} - \boldsymbol{\Lambda} (\boldsymbol{n} - \boldsymbol{n}^{eq}) + \delta_t \boldsymbol{Q}, \tag{16}$$

where $\boldsymbol{n} = \boldsymbol{M}\boldsymbol{g}$ with $\boldsymbol{n} = (n_0^*, n_1^*, ..., n_8^*)^{\mathrm{T}}$ and $\boldsymbol{n}^{eq} = \boldsymbol{M}\boldsymbol{g}^{eq}$, in which $\boldsymbol{g} = (g_0, g_1, ..., g_8)^{\mathrm{T}}$ and the equilibrium distribution $\boldsymbol{g}^{eq} = (g_0^{eq}, g_1^{eq}, \cdots, g_8^{eq})^{\mathrm{T}}$. In the D2Q9 model, $\boldsymbol{n}^{eq}$ are given by

$$\boldsymbol{n}^{eq} = T (1, \quad -2, \quad 2, \quad v_x{}' \quad -v_x{}' \quad v_y, \quad -v_y{}' \quad 0, \quad 0)^T. \tag{17}$$

$\boldsymbol{Q}$ is the source term in the momentum space, which is shown as

$$\boldsymbol{Q} = (Q_0, \quad 0, \quad 0, \quad 0, \quad 0, \quad 0, \quad 0, \quad 0, \quad 0)^T, \tag{18}$$

where $Q_0 = \phi + 0.5\delta_t \partial_t \phi$. According Ref. (Chopard et al., 2009), in the numerical implementation, **Eq. 18** is calculated with $\partial_t \phi \approx \frac{[\phi(t) - \phi(t - \delta_t)]}{\delta_t}$.

The streaming process of temperature function is similar to **Eq. 7**

$$g_\alpha (\boldsymbol{x} + \boldsymbol{e}_\alpha \delta_t, t + \delta_t) = g_\alpha^* (\boldsymbol{x}, t), \tag{19}$$

where $g^* = \boldsymbol{M}^{-1} \boldsymbol{m}^*$. It should be emphasized that the unit used in this work is the LBM lattice unit. The length's unit is *lu*, time step's unit is *ts* and the unit of mass is *mu*. The units of velocity, density, pressure, and viscosity are given as *lu/ts*, *mu/lu*^{3}, *mu/(ts^{2}lu)* and *lu^2/ts*, respectively.

MODEL VALIDATION

Laplace's Law

Laplace's law states that in the case of cavitation bubbles, the pressure difference between inside and outside the bubble is inversely proportional to the bubble radius, which is shown as
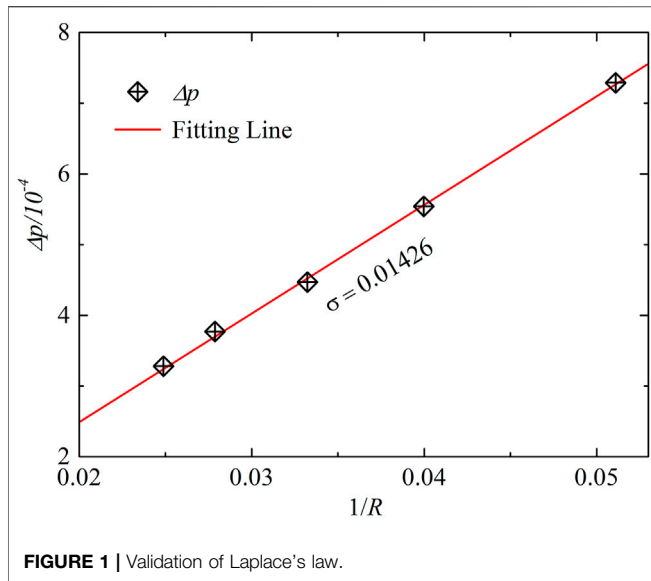
FIGURE 1 | Validation of Laplace's law.

$$\Delta p = p_{in} - p_{out} = \frac{\sigma}{R}, \tag{20}$$

where p_{in} indicates the pressure inside the bubble, p_{out} indicates the pressure outside the bubble, σ represents the surface tension, and R is the equilibrium radius of the bubble. A spherical bubble in the liquid domain is located in the center of a periodic field without gravity. The initial density field formula is (Shan et al., 2016)

$$\rho(x, y) = \frac{\rho_{in} + \rho_{out}}{2}$$
$$+ \frac{\rho_{in} - \rho_{out}}{2} \times tan\,h\left[\frac{2\left(\sqrt{(x - x_0)^2 + (y - y_0)^2} - R\right)}{W}\right], \tag{21}$$

where $tan\,h(x) = (e^{2x} - 1)/(e^{2x} + 1)$ is the hyperbolic tangent function. ρ_{in} represents the density inside the bubble and ρ_{out} represents the density outside the bubble. The width of the phase interface $W = 5$. (x_0, y_0) is the central coordinates of the 401 × 401 lattice system. At dimension temperature $0.85T_c$, the initial vapor and liquid density are approximately equal to the 0.34 and 6.6. The initial bubble radius R_0 is set as 20, 30, 40, 50 and 60. It can be clearly observed from **Figure 1** that the direct proportionality of the pressure difference Δp to the inverse radius $1/R$, indicating that the simulation results are in good agreement with Laplace's law.

Validation of Rayleigh-Plesset Equation and Temperature Equation

As is well known, the bubble dynamics equation in a viscous fluid—i.e., the R–P equation—is (Brennen, 1973)

$$R\ddot{R} + \frac{3}{2}\dot{R}^2 = \frac{1}{\rho_l}\left[\left(p_\infty + \frac{2\sigma}{R} - p_v\right)\left(\frac{R_0}{R}\right)^{3\gamma} + p_v - p_\infty - \frac{4\mu\dot{R}}{R} - \frac{2\sigma}{R}\right], \tag{22}$$

where p_v is the vapor pressure in the bubble, p_∞ is the liquid pressure. Dots represent time derivative: $\dot{R} = dR/dt$, $\ddot{R} = d^2R/dt^2$. γ is the adiabatic coefficient. $\mu = (\tau_v - \frac{1}{2})c_s^2\delta t$ is dynamic viscosity. In order to compare this simulation result with the numerical solution and R-P equation solution, the corresponding LBM parameters are substituted into **Eq. 22** to obtain the solution of the R-P equation. The pressure difference $\Delta p = p_\infty - p_v = 0.0853$ obtained is used to trigger the collapse of the bubble. The initial densities of vapor and liquid are $\rho_v \approx 0.34$ and $\rho_l \approx 6.6$ at $0.85T_c$, respectively. The size of the numerical simulation domain is 401 × 401, and the periodic boundary conditions are used in all directions. The time is dimensionless throughout the simulation time step. The bubble radius is normalized to the initial radius R_0. As shown in **Figure 2**, the simulation results are consistent with the numerical results of the R-P equation. The correctness of the improved pseudopotential thermal MRT LB model is verified.

The temperature formula of the cavitation bubble, deduced from the R–P equation, is

$$T = T_\infty\left(\frac{R_0}{R}\right)^{3(\gamma-1)}, \tag{23}$$

where T_∞ indicates the ambient temperature of the liquid, and $\gamma = 1.3$ is a constant representing the adiabatic coefficient. In our simulation, periodic boundary conditions are adopted in all directions. The liquid temperature $T_\infty = 0.85T_c$ is considered uniform. The pressure difference $\Delta p = p_\infty - p_v$. The instantaneous temperature T is normalized, and the $t^\star$ is dimensionless throughout the simulation time step.

The current theoretical results show that the maximum collapse temperature of the bubble is infinite. What prevents such a runaway increase is heat dissipation, viscous dissipation and other uncontrollable factors in experiments or numerical
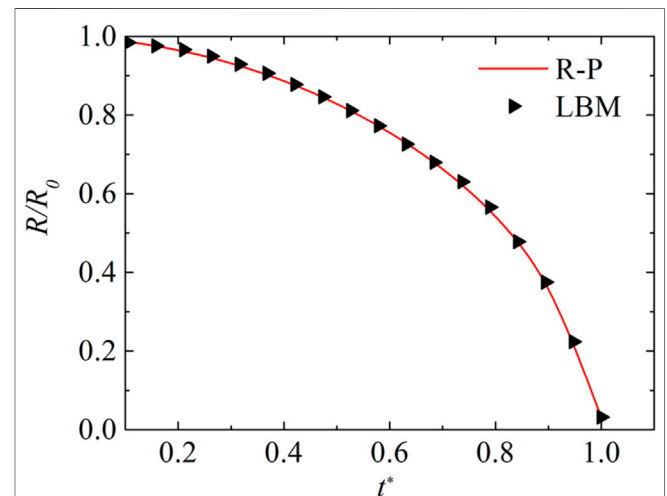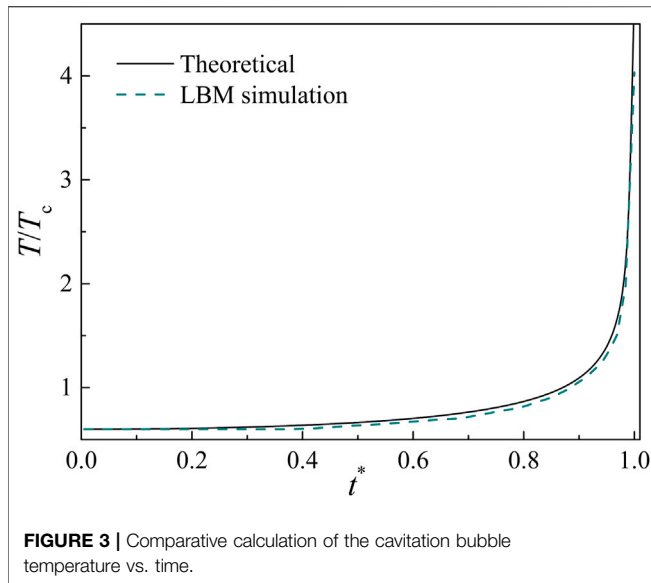

FIGURE 2 | Evolution curve of collapsed bubble radius.

FIGURE 3 | Comparative calculation of the cavitation bubble temperature vs. time.

simulations. As shown in **Figure 3**, the simulation results closely track the theoretical solution results, supporting the reliability of the present model. The thermal LB model can therefore be used to predict and analyze the collapse of cavitation bubble near solid wall.

NUMERICAL RESULTS

Model Establishment

As illustrated in **Figure 4**, numerical simulation is carried out in the two-dimensional x-y plane, and the computational domain $l_x \times l_y$. The nonslip boundary scheme (Mohamad, 2017) is applied at the wall that is defined at $y = 0$ and periodic boundaries are utilized in the horizontal direction. The top of the computational domain is set as an open boundary, and the anti-bounce-back approach is applied. In our simulation, the initial radius of the bubble is R_0, b denotes the distance from the center of the bubble to the solid wall, and $\lambda = \frac{b}{R_0}$ is defined as the offset parameter. The initial equilibrium temperature is taken as $T_\infty = 0.85T_c$, corresponding to the coexistence densities $\rho_v \approx 0.34$ and $\rho_l \approx 6.63$.

Bubble Profile and Grid Independent Validation

Figure 5 shows the comparison between the current bubble profile and the results of an underwater pulsed discharge experiments published in the literature (Shan et al., 2019). Due to the difference in the size of the cavitation bubbles in the experimental study and numerical simulation, their collapse time cannot be directly compared and needs to be normalized. Comparing the **Figures 5A,B**, it can be found that the morphological evolution process of the bubble is consistent, and the dimensionless time obtained after normalization is the same. The result verifies the correctness of the LBM numerical experiment from the appearance change of the bubble.

In addition, in order to make a more accurate comparison and prove the symmetry of the collapse of cavitation bubble near the solid wall, the grid independence verification is carried out in this section. First the coordinates of the bubble surface need to be obtained. The criterion for the interface between the vapor and the liquid is that the density of the interface point is equal to $(\rho_{v+}\rho_l)/2$. We chose 301×301, 401×401 and 501×501 grids, according to the principle of the same scale, the initial bubble radii are 60, 80, and 100, respectively. The dimensionless time T^* is defined, which represents the time from the initial state to the first collapse. The bubble contour points of 0, $0.2T^*$, $0.4T^*$, $0.6T^*$, $0.8T^*$, and T^* under three grid resolutions are extracted, and the coordinate points obtained in the x and y directions are dimensionless, as shown in **Figure 6**. The result shows that the normalized contours of cavitation bubble collapse near the wall almost coincide with each other of the three grid resolutions, which indicates that the numerical model of cavitation bubble collapse near the wall is independent of the grid size. Considering the computational efficiency and the observability of the results, we choose 401×401 grids for the following numerical experiments.

Collapse Evolution Process of Cavitation Bubble Near a Wall

Figure 7 shows the evolution of the temperature, pressure and fluid velocity fields of a single cavitation bubble collapse near the solid wall (prior to complete collapse). Due to the left-right symmetry of the entire system, in the evolution result image, the left side is the pressure field and the fluid velocity field, and the right side is the temperature field. As shown in **Figures 7A,B**, the spherical cavitation bubble is deformed into an elongated bubble in the direction perpendicular to the solid wall. The fluid velocity above the bubble is relatively high, which leads to a higher temperature in the liquid area and the area above the bubble. The near-wall fluid velocity is lower, causing the temperature in
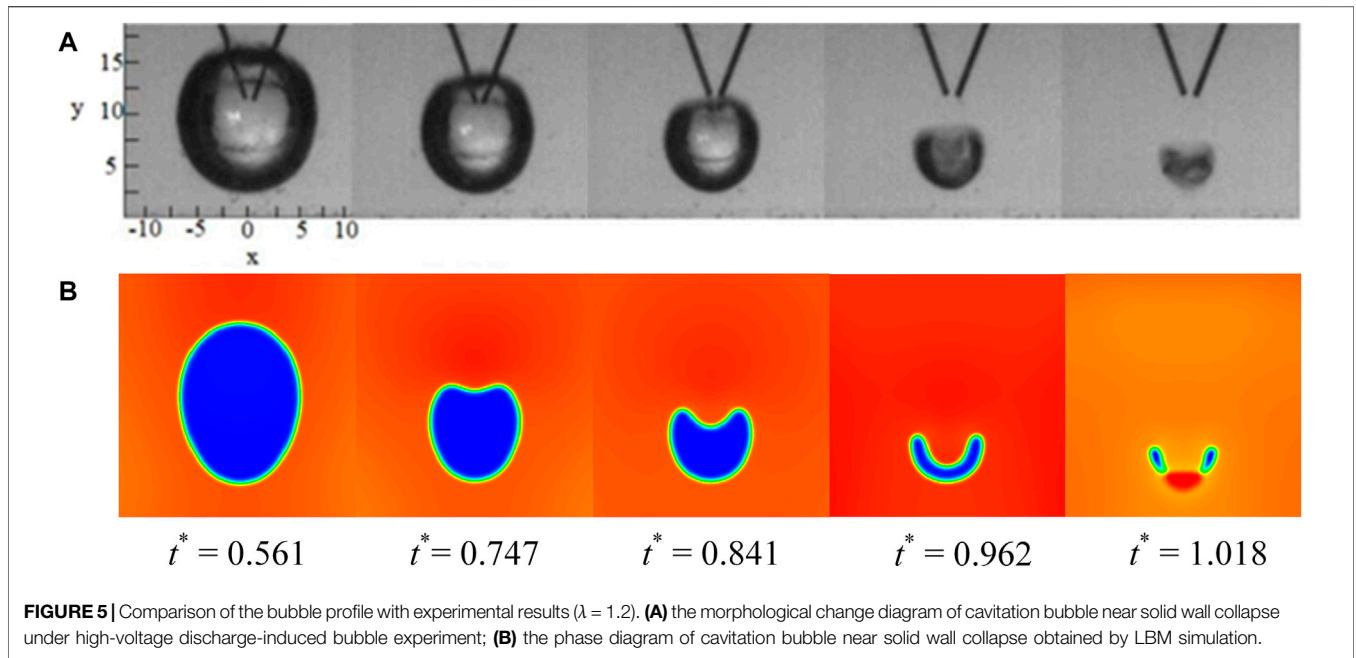

FIGURE 4 | Computational domain.
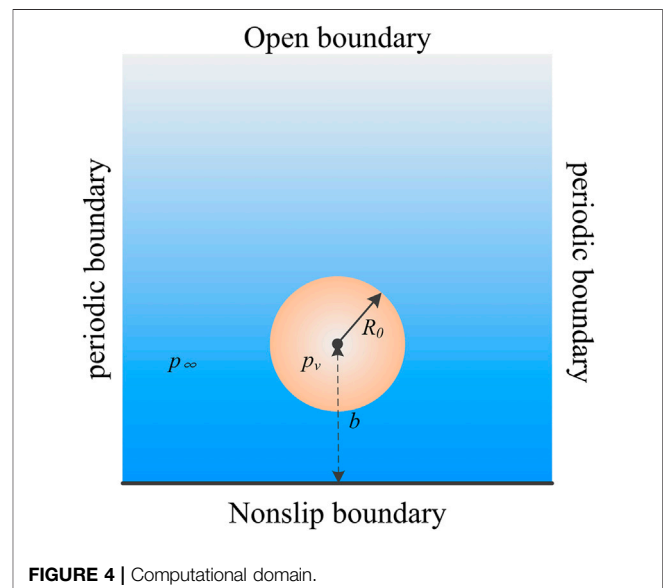
FIGURE 5 | Comparison of the bubble profile with experimental results (λ = 1.2). **(A)** the morphological change diagram of cavitation bubble near solid wall collapse under high-voltage discharge-induced bubble experiment; **(B)** the phase diagram of cavitation bubble near solid wall collapse obtained by LBM simulation.
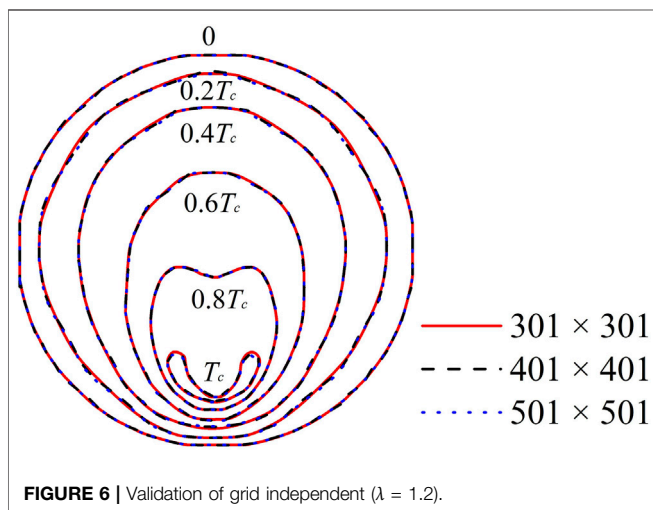

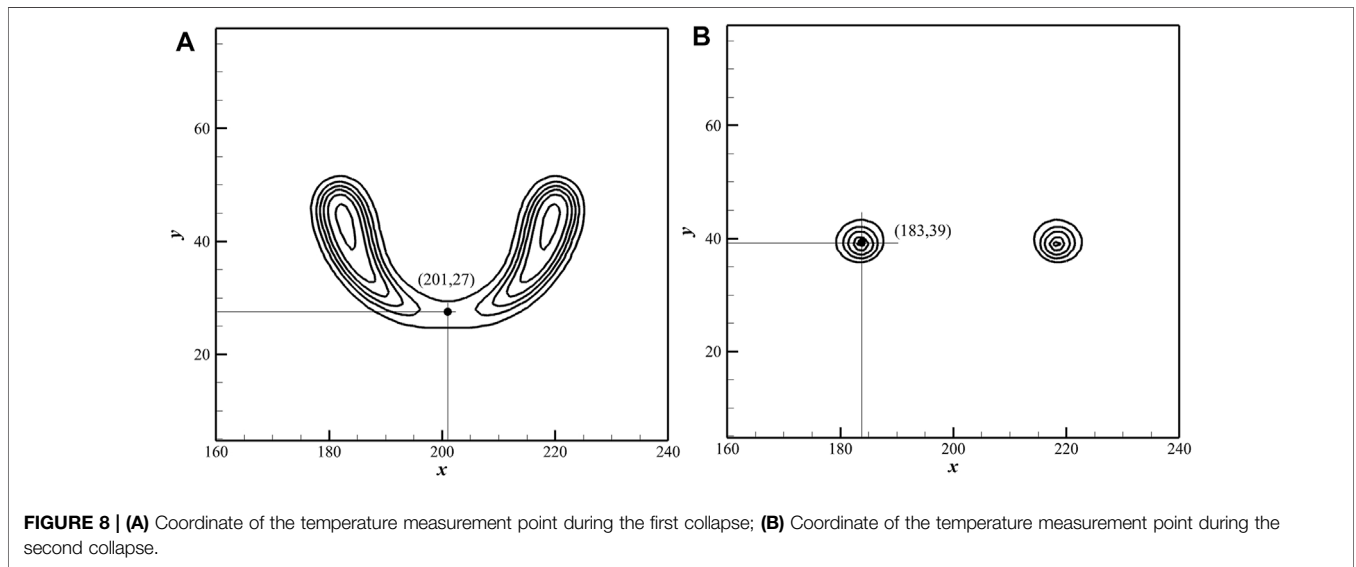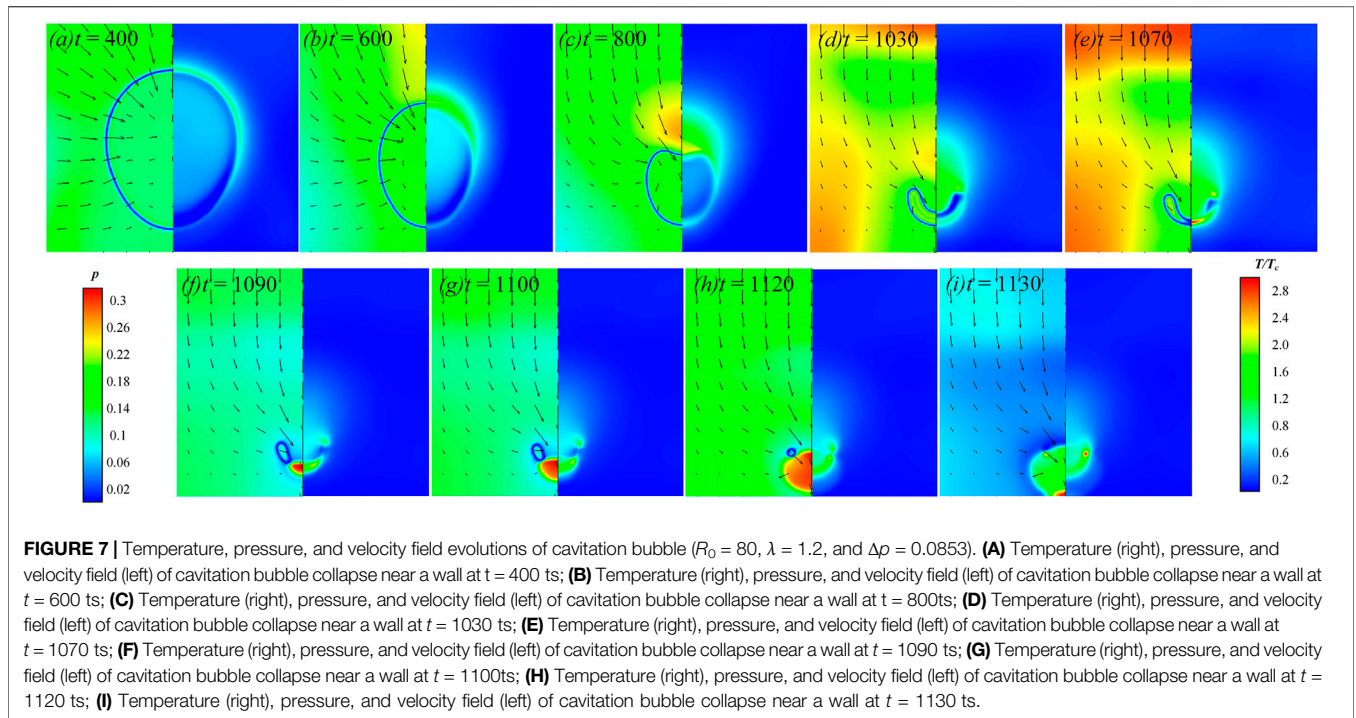**FIGURE 6 |** Validation of grid independent (λ = 1.2).

the bottom area of the bubble to decrease. As can be seen from **Figures 7C,D**, the micro-jet formed above the bubble causes local liquid pressure fluctuations and makes the local fluid particles vibrate rapidly. A thermal boundary layer forms at the bubble surface. **Figure 7E** shows the first collapse of the bubble, where the micro-jet impinges on the bottom edge of the bubble and the bubble temperature rises instantaneously. After the first collapse, a shock wave is emitted toward the solid wall and forms a hot spot on the wall, as has been discussed in Refs. (Yang et al., 2020) and (Yang et al., 2021). As shown in **Figure 7F**, the bubble becomes toroidal and its internal initial temperature is low. Then the toroidal bubble collapses rapidly under the driving action of the micro-jet, that is, the second collapse of the bubble. It can be seen from the time steps of **Figure 7F**-(i) that the second collapse of

the bubble is very fast. The toroidal bubble temperature increases sharply and reaches a maximum when the bubble collapses completely.

From previous work, we know that the bubble temperature affected by the nondimensional offset parameter λ, initial pressure difference Δp and initial bubble radius R_0. In order to understand the evolution results of the bubble temperature, the following sections discuss and analyze the above-mentioned factors in detail.
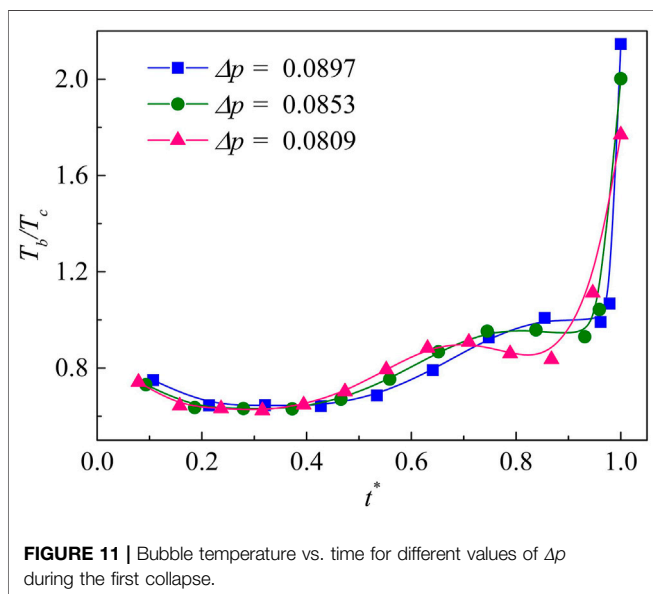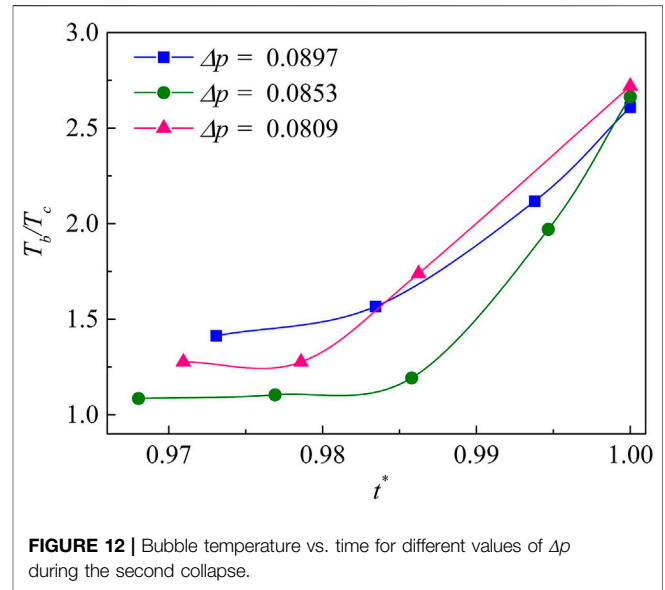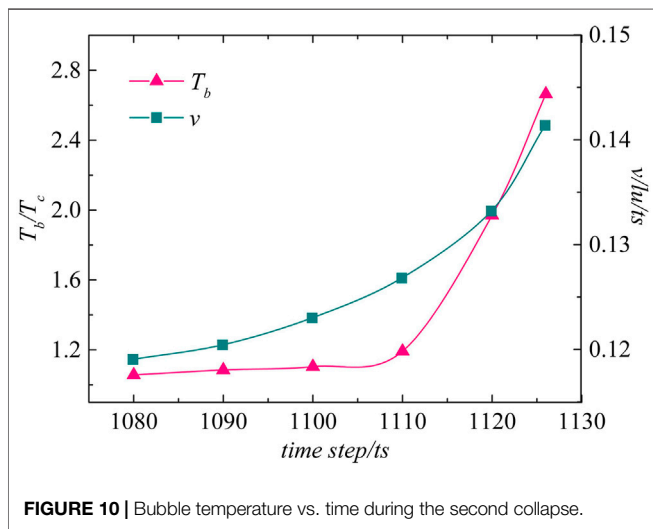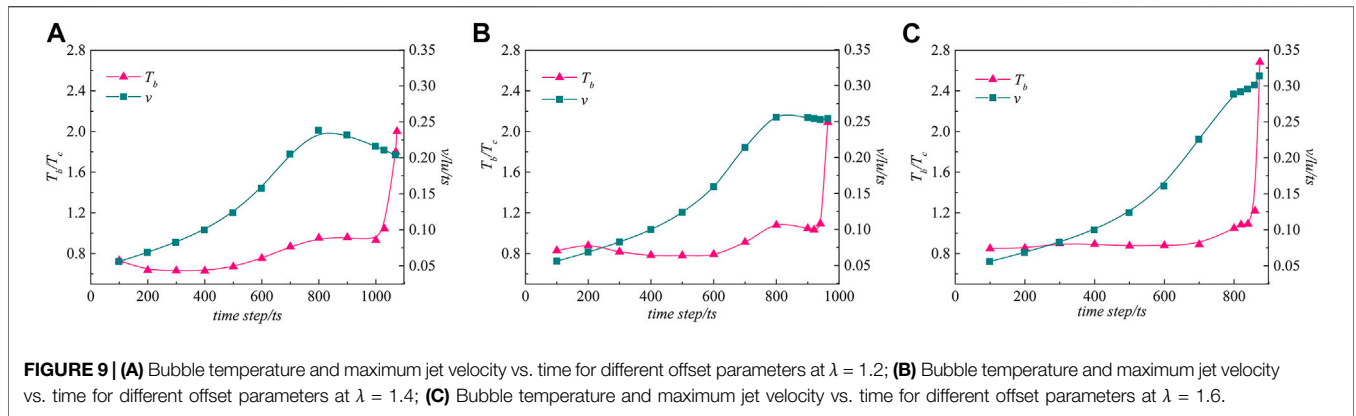
Analysis of Different Offset Parameters

In this section, the effect of the different offset parameters on the bubble temperature will be discussed. Since the temperature distribution in the bubble is not uniform, we take a certain point inside the bubble as the temperature measurement point. For example, when λ = 1.2, as shown in **Figure 8A**, the coordinates of the measurement point are (201, 27). This is a point located at the bottom of the bubble on the vertical bisector of the x axis. For other values of λ, the temperature measurement point can be obtained by the same way. **Figure 9** shows the bubble temperature curves with offset parameters of 1.2, 1.4 and 1.6. In order to explain the changes of the bubble temperature more clearly, the maximum jet velocity of the perpendicular bisectors of the x axis under three offset parameters is also shown in **Figure 8**. The initial conditions and parameter settings of the three cases are the same. In **Figure 9A**, the bubble temperature decreases slightly during the bubble shrinkage stage, which is caused by the lower pressure of the bottom liquid and lower velocity. With the formation of the micro jet, the maximum jet velocity accelerates gradually, and the bubble temperature also increases. Then, the jet velocity decreases after reaching its maximum, which is impeded by the deforming bubble. Meantime, the bubble temperature drops briefly and rises sharply at the first

FIGURE 7 | Temperature, pressure, and velocity field evolutions of cavitation bubble (R_0 = 80, λ = 1.2, and Δp = 0.0853). **(A)** Temperature (right), pressure, and velocity field (left) of cavitation bubble collapse near a wall at t = 400 ts; **(B)** Temperature (right), pressure, and velocity field (left) of cavitation bubble collapse near a wall at t = 600 ts; **(C)** Temperature (right), pressure, and velocity field (left) of cavitation bubble collapse near a wall at t = 800ts; **(D)** Temperature (right), pressure, and velocity field (left) of cavitation bubble collapse near a wall at t = 1030 ts; **(E)** Temperature (right), pressure, and velocity field (left) of cavitation bubble collapse near a wall at t = 1070 ts; **(F)** Temperature (right), pressure, and velocity field (left) of cavitation bubble collapse near a wall at t = 1090 ts; **(G)** Temperature (right), pressure, and velocity field (left) of cavitation bubble collapse near a wall at t = 1100 ts; **(H)** Temperature (right), pressure, and velocity field (left) of cavitation bubble collapse near a wall at t = 1120 ts; **(I)** Temperature (right), pressure, and velocity field (left) of cavitation bubble collapse near a wall at t = 1130 ts.

FIGURE 8 | (A) Coordinate of the temperature measurement point during the first collapse; **(B)** Coordinate of the temperature measurement point during the second collapse.

collapse. In **Figure 9B**, the trend of the bubble temperature curve is similar to that of **Figure 9A**, and the jet velocity decreases slightly before the first collapse. The maximum bubble temperature is higher than in **Figure 9A**. However, as shown in **Figure 9C**, the jet velocity keeps increasing in the early stages of the collapse, and the acceleration of the final stage of the collapse decreases. The bubble temperature increases as λ increases and reaches the greatest value when λ = 1.6. It can be inferred that the larger is λ, the higher is the maximum bubble temperature. In addition, we find that the cavitation bubble will become toroidal

when λ = 1.2 after the first collapse. The bubble collapses directly without becoming toroidal when λ = 1.4 or 1.6 (i.e., when it is farther from the wall). As shown in **Figure 8B**, the coordinates of the temperature measurement point of the toroidal bubble are (183, 39). **Figure 10** shows the evolution of the toroidal bubble temperature and the maximum jet velocity around the bubble from the second collapse to complete collapse. Due to the driving effect of the jet and the water hammer effect, the jet velocity increases rapidly, and the toroidal bubble collapses and produces high temperature almost instantaneously.

FIGURE 9 | (A) Bubble temperature and maximum jet velocity vs. time for different offset parameters at $\lambda = 1.2$; **(B)** Bubble temperature and maximum jet velocity vs. time for different offset parameters at $\lambda = 1.4$; **(C)** Bubble temperature and maximum jet velocity vs. time for different offset parameters at $\lambda = 1.6$.

FIGURE 10 | Bubble temperature vs. time during the second collapse.

FIGURE 12 | Bubble temperature vs. time for different values of Δp during the second collapse.

FIGURE 11 | Bubble temperature vs. time for different values of Δp during the first collapse.

Analysis of Different Driving Pressures and Bubble Radii

In this section, the influences of the initial driving pressure and bubble radius are studied. Because the collapse time is different for different Δp and different initial radius R0, the time step is normalized in the following section for comparison. **Figure 11** shows the bubble temperature vs. time during the first collapse for three different values of initial Δp. The result shows that there is no obvious dependence of temperature on Δp at the bubble contraction stage. As Δp increases, the bubble temperature increases gradually. Then the bubble temperature drops briefly, as shown in more detail in **Figure 9A**, the bubble temperature is related to the jet velocity. Due to the impeding effect of the bubble, the jet velocity decreases briefly, causing the bubble temperature to drop. One may note that, the smaller Δp, the more significant the temperature drop. When the bubble collapses for the first time, its temperature increases dramatically. For $\Delta p = 0.0897$, the bubble temperature rises fastest and to the greatest value. It can be concluded that the

FIGURE 13 | Bubble temperature vs. time during the first collapse for several values of R_0.
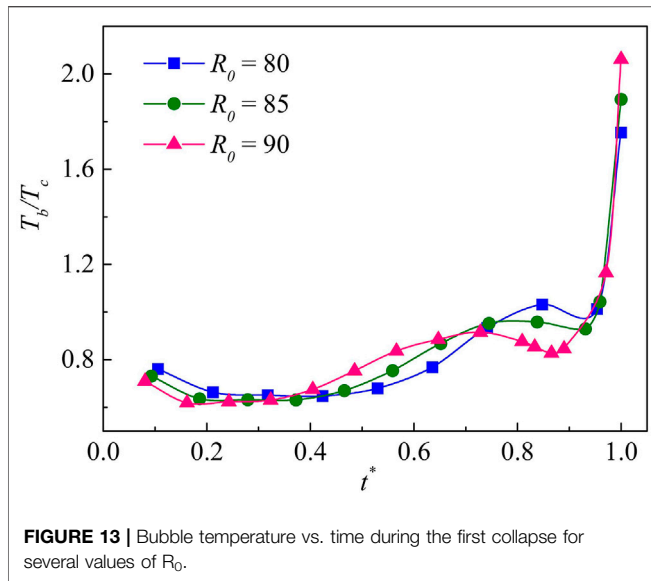
large pressure difference has large potential energy, which releases more energy when collapsing leading to a higher temperature. The bubble becomes toroidal after the first collapse in all three cases. **Figure 12** shows the time-dependence of the toroidal bubble temperature. The initial toroidal temperature is low; it increases gradually as the bubble collapses and eventually reaches a maximum. The collapse temperature is almost the same as that of the three Δp. It can be inferred that the pressure difference has little effect on the toroidal bubble temperature during the second collapse.

The evolutions of the bubble temperature during the cavitation bubble collapse with initial radii of 80, 85 and 90 and with an initial driving pressure $\Delta p = 0.0853$ are shown in **Figure 13**. It can be seen that the bubble temperature rises

FIGURE 14 | Toroidal temperature vs. time during the second collapse for several values of R_0.
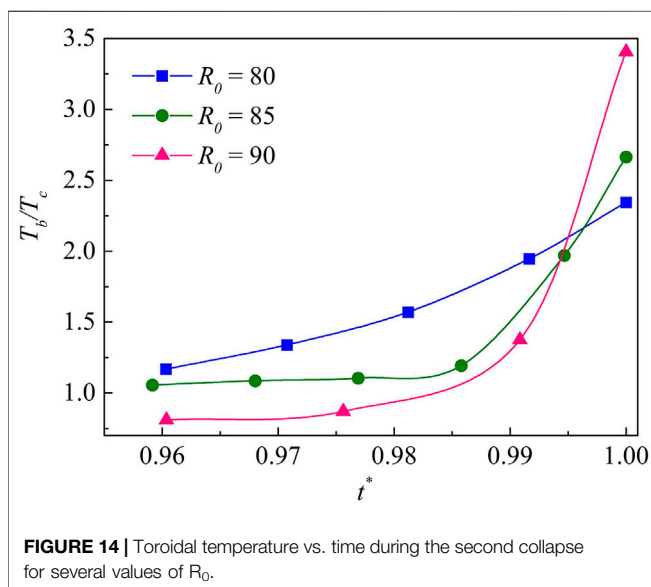
gradually after a brief cooling. When $R_0 = 90$, the larger value, the bubble temperature drops significantly. The bubble temperature then increases sharply when the bubble collapses for the first time. The larger the bubble radius, the greater is the internal energy, and the more energy is released when the bubble collapses, which leads to higher bubble temperature.

The bubble becomes toroidal after the first collapse. In **Figure 14**, the bubble temperature of the newly formed toroidal bubble is the lowest among these three examples when $R_0 = 90$, but for the value of R0 the final temperature is the highest, with the most drastic bubble temperature change. For larger initial radius, the maximum bubble temperature is therefore higher at the second collapse.

CONCLUSION

In this paper, the validation of the Laplace's law, R-P equation and temperature equation are verified, and the simulation results of cavitation bubble collapse near the wall are consistent with the experimental results. Using a thermal multiphase lattice Boltzmann model with liquid-vapor phase change, we have numerically investigated the temperature evolution characteristics of a cavitation bubble collapsing near the wall. The main findings and conclusion are summarized as follows.

1) The temperature distribution in the bubble varies with the external liquid pressure and velocity. At the initial stage of the bubble collapse, the temperature in the upper region of the bubble increases due to greater jet velocity and pressure in this region. At the same time, the temperature in the bottom region of the bubble decreases because the jet velocity and pressure field near the wall are low. The simulation results show that the bubble temperature is highly dependent on the jet velocity and the pressure field.

2) The offset parameter affects the change of temperature inside the bubble. The results show that the bubble hit by a jet generates high temperature almost instantly. The larger is λ, the higher is maximum bubble temperature. When λ is smaller—for example, when $\lambda = 1.2$—the bubble becomes toroidal after the first collapse, and high temperature is generated in the bubble due to the driving effect of pressure and water hammer effect when the toroidal bubble collapses completely.

3) The initial driving pressure and initial bubble radius also have an effect on the bubble temperature. 1) During the first collapse, the larger the initial Δp, the greater is bubble temperature. A large pressure difference has large potential energy, which causes the bubble to release more energy when it collapses, thus increasing the bubble temperature. The second collapse, of the toroidal bubble, is mainly governed by the water hammer effect and the jet rebound effect. The initial driving pressure Δp has little effect on the toroidal bubble. 2) The greater the initial bubble radius, the higher is the bubble temperature. Large bubble contains large internal

energy, and will release more energy when the bubble collapses, resulting in higher bubble temperature.

We believe that the present simulations are useful for understanding the internal mechanisms of the cavitation bubble temperature and its effects. Moreover, the investigation of the temperature evolution and distribution in the bubble provide insights to assists in the further research and applications on the thermodynamics of cavitation bubbles.

DATA AVAILABILITY STATEMENT

The original contributions presented in the study are included in the article/Supplementary Material, further inquiries can be directed to the corresponding author.

REFERENCES

AUTHOR CONTRIBUTIONS

All authors contributed extensively to this work. YY performed the simulation, data analysis, and wrote the paper. MS conceived, supervised and revised the manuscript the project the study. XK and FS drew the figures and revised the manuscript. MS and QH directed the study, supervised the project.

Biferale, L., Perlekar, P., Sbragaglia, M., and Toschi, F. (2012). Convection in Multiphase Fluid Flows Using Lattice Boltzmann Methods. *Phys. Rev. Lett.* 108, 104502. doi:10.1103/PhysRevLett.108.104502

Biferale, L., Perlekar, P., Sbragaglia, M., and Toschi, F. (2013). Simulations of Boiling Systems Using a Lattice Boltzmann Method. *Commun. Comput. Phys.* 13, 696–705. doi:10.4208/cicp.321011.020212s

Brennen, C. E. (2005). *Fundamentals of Multiphase Flow*. Cambridge University Press, 19–22.

Brennen, C. (1973). The Dynamic Behavior and Compliance of a Stream of Cavitating Bubbles. *J. Fluids Eng.* 95, 533–541. doi:10.1115/1.3447067

Cervone, A., Testa, R., Bramanti, C., Rapposelli, E., and d'Agostino, L. (2005). Thermal Effects on Cavitation Instabilities in Helical Inducers. *J. Propulsion Power* 21, 893–899. doi:10.2514/1.12582

Chahine, G. L., and Hsiao, C.-T. (2015). Modelling Cavitation Erosion Using Fluid-Material Interaction Simulations. *Interf. Focus.* 5, 20150016. doi:10.1098/rsfs.2015.0016

Chopard, B., Falcone, J. L., and Latt, J. (2009). The Lattice Boltzmann Advection-Diffusion Model Revisited. *Eur. Phys. J. Spec. Top.* 171, 245–249. doi:10.1140/epjst/e2009-01035-5

Dong, Z., Li, W., and Song, Y. (2009). Lattice Boltzmann Simulation of Growth and Deformation for a Rising Vapor Bubble through Superheated Liquid. *Numer. Heat Transfer, A: Appl.* 55, 381–400. doi:10.1080/10407780902720718

Dular, M., and Coutier-Delgosha, O. (2013). Thermodynamic Effects during Growth and Collapse of a Single Cavitation Bubble. *J. Fluid Mech.* 736, 44–66. doi:10.1017/jfm.2013.525

Flannigan, D. J., and Suslick, K. S. (2005). Plasma Formation and Temperature Measurement during Single-Bubble Cavitation. *Nature* 434, 52–55. doi:10.1038/nature03361

Fujikawa, S., Okuda, M., Akamatsu, T., and Goto, T. (2006). Non-equilibrium Vapour Condensation on a Shock-Tube Endwall behind a Reflected Shock Wave. *J. Fluid Mech.* 183, 293–324. doi:10.1017/S0022112087002647

Gan, Y., Xu, A., Zhang, G., and Succi, S. (2015). Discrete Boltzmann Modeling of Multiphase Flows: Hydrodynamic and Thermodynamic Non-equilibrium Effects. *Soft Matter* 11, 5336–5345. doi:10.1039/c5sm01125f

Gavranek, V. V., Bol'shutkin, D. N., and Zel'dovich, V. I. (1960). Thermal and Mechanical Action of a Cavitation Zone on the Surface of a Metal. *Fiz. Metal Metalloved* 10, 262–268.

Gong, S., and Cheng, P. (2012). A Lattice Boltzmann Method for Simulation of Liquid-Vapor Phase-Change Heat Transfer. *Int. J. Heat Mass Transfer* 55, 4923–4927. doi:10.1016/j.ijheatmasstransfer.2012.04.037

Gonnella, G., Lamura, A., and Sofonea, V. (2007). Lattice Boltzmann Simulation of thermal Nonideal Fluids. *Phys. Rev. E* 76, 036703. doi:10.1103/PhysRevE.76.036703

Guo, Z., Shi, B., and Zheng, C. (2002). A Coupled Lattice BGK Model for the Boussinesq Equations. *Int. J. Numer. Meth. Fluids* 39, 325–342. doi:10.1002/fld.337

Házi, G., and Márkus, A. (2008). Modeling Heat Transfer in Supercritical Fluid Using the Lattice Boltzmann Method. *Phys. Rev. E* 77, 026305. doi:10.1103/PhysRevE.77.026305

He, X., Chen, S., and Doolen, G. D. (1998). A Novel thermal Model for the Lattice Boltzmann Method in Incompressible Limit. *J. Comput. Phys.* 146, 282–300. doi:10.1006/jcph.1998.6057

He, X., Chen, S., and Zhang, R. (1999). A Lattice Boltzmann Scheme for Incompressible Multiphase Flow and its Application in Simulation of Rayleigh-Taylor Instability. *J. Comput. Phys.* 152, 642–663. doi:10.1006/jcph.1999.6257

Huai, X., Yan, R., Cai, J., and Li, X. (2011). Dynamic Analysis on Temperature Evolution inside a Single Bubble Due to Hydrodynamic Cavitation under Turbulence. *Chin. Sci. Bull.* 56, 947–955. doi:10.1360/972010-1722

Lallemand, P., and Luo, L.-S. (2000). Theory of the Lattice Boltzmann Method: Dispersion, Dissipation, Isotropy, Galilean Invariance, and Stability. *Phys. Rev. E* 61, 6546–6562. doi:10.1103/PhysRevE.61.6546

Li, Q., Luo, K. H., Kang, Q. J., He, Y. L., Chen, Q., and Liu, Q. (2016). Lattice Boltzmann Methods for Multiphase Flow and Phase-Change Heat Transfer. *Prog. Energ. Combustion Sci.* 52, 62–105. doi:10.1016/j.pecs.2015.10.001

Li, Q., Luo, K. H., and Li, X. J. (2012). Forcing Scheme in Pseudopotential Lattice Boltzmann Model for Multiphase Flows. *Phys. Rev. E* 86, 016709. doi:10.1103/PhysRevE.86.016709

Li, Q., Luo, K. H., and Li, X. J. (2013). Lattice Boltzmann Modeling of Multiphase Flows at Large Density Ratio with an Improved Pseudopotential Model. *Phys. Rev. E* 87, 053301. doi:10.1103/PhysRevE.87.053301

Li, Q., Zhou, P., and Yan, H. J. (2017). Improved thermal Lattice Boltzmann Model for Simulation of Liquid-Vapor Phase Change. *Phys. Rev. E* 96, 063303. doi:10.1103/PhysRevE.96.063303

Liu, X., and Cheng, P. (2013). Lattice Boltzmann Simulation of Steady Laminar Film Condensation on a Vertical Hydrophilic Subcooled Flat Plate. *Int. J. Heat Mass Transfer* 62, 507–514. doi:10.1016/j.ijheatmasstransfer.2013.03.002

Márkus, A., and Házi, G. (2011). Simulation of Evaporation by an Extension of the Pseudopotential Lattice Boltzmann Method: a Quantitative Analysis. *Phys. Rev. E* 83, 046705. doi:10.1103/PhysRevE.83.046705

Mason, T. J. (2016). Ultrasonic Cleaning: an Historical Perspective. *Ultrason. Sonochem.* 29, 519–523. doi:10.1016/j.ultsonch.2015.05.004

Meullemiestre, A., Breil, C., Abert-Vian, M., and Chemat, F. (2017). Manothermosonication as a Useful Tool for Lipid Extraction from Oleaginous Microorganisms. *Ultrason. Sonochem.* 37, 216–221. doi:10.1016/j.ultsonch.2017.01.014

Mohamad, A. (2017). *The Lattice Boltzmann Method*. Springer International Publishing.

Nowotny, H. (1942). *Destruction of Materials by Cavitation*. VDI-Verlag.

Ohl, C.-D., Arora, M., Dijkink, R., Janve, V., and Lohse, D. (2006). Surface Cleaning from Laser-Induced Cavitation Bubbles. *Appl. Phys. Lett.* 89, 074102–0741023. doi:10.1063/1.2337506

Safari, H., Rahimian, M. H., and Krafczyk, M. (2010). Extended Lattice Boltzmann Method for Numerical Simulation of thermal Phase Change in Two-phase Fluid Flow. *Phys. Rev. E* 88, 036707. doi:10.1103/PhysRevE.88.013304

Sbragaglia, M., Benzi, R., Biferale, L., Succi, S., Sugiyama, K., and Toschi, F. (2007). Generalized Lattice Boltzmann Method with Multirange Pseudopotential. *Phys. Rev. E* 75, 026702. doi:10.1103/PhysRevE.75.026702

Shan, M.-L., Zhu, C.-P., Yao, C., Yin, C., and Jiang, X.-Y. (2016). Pseudopotential Multi-Relaxation-Time Lattice Boltzmann Model for Cavitation Bubble Collapse with High Density Ratio. *Chin. Phys. B* 25, 104701. doi:10.1088/1674-1056/25/10/104701

Shan, M., Chen, B., Yao, C., Han, Q., Zhu, C., and Yang, Y. (2019). Electric Characteristic and Cavitation Bubble Dynamics Using Underwater Pulsed Discharge. *Plasma Sci. Technol.* 21, 074002. doi:10.1088/2058-6272/ab0b62

Shan, M., Yang, Y., Peng, H., Han, Q., and Zhu, C. (2017). Modeling of Collapsing Cavitation Bubble Near Solid wall by 3D Pseudopotential Multi-Relaxation-Time Lattice Boltzmann Method. *Proc. Inst. Mech. Eng. C: J. Mech. Eng. Sci.* 232, 445–456. doi:10.1177/0954406217740167

Shan, X. (2006). Analysis and Reduction of the Spurious Current in a Class of Multiphase Lattice Boltzmann Models. *Phys. Rev. E* 73, 047701. doi:10.1103/PhysRevE.73.047701

Shan, X. (2008). Pressure Tensor Calculation in a Class of Nonideal Gas Lattice Boltzmann Models. *Phys. Rev. E* 77, 066702. doi:10.1103/PhysRevE.77.066702

Suslick, K. S., Eddingsaas, N. C., Flannigan, D. J., Hopkins, S. D., and Xu, H. (2011). Extreme Conditions during Multibubble Cavitation: Sonoluminescence as a Spectroscopic Probe. *Ultrason. Sonochem.* 18, 842–846. doi:10.1016/j.ultsonch.2010.12.012

Suslick, K. S., and Flannigan, D. J. (2008). Inside a Collapsing Bubble: Sonoluminescence and the Conditions during Cavitation. *Annu. Rev. Phys. Chem.* 59, 659–683. doi:10.1146/annurev.physchem.59.032607.093739

Tomita, Y., and Shima, A. (1986). Mechanisms of Impulsive Pressure Generation and Damage Pit Formation by Bubble Collapse. *J. Fluid Mech.* 169, 535–564. doi:10.1017/S0022112086000745

Verhaagen, B., and Fernández Rivas, D. (2016). Measuring Cavitation and its Cleaning Effect. *Ultrason. Sonochem.* 29, 619–628. doi:10.1016/j.ultsonch.2015.03.009

Wang, Z. C., Zhang, Y., and Zhang, X. Q. (2001). The thermal Effect during Cavitation Erosion. *Chin. Mater. Res.* 15, 287–290.

Yang, Y., Shan, M.-L., Han, Q.-B., and Kan, X.-F. (2021). Effect of Non-condensable Gas on a Collapsing Cavitation Bubble Near Solid wall Investigated by Multicomponent thermal MRT-LBM*. *Chin. Phys. B* 30, 024701. doi:10.1088/1674-1056/abbbf8

Yang, Y., Shan, M., Kan, X., Shangguan, Y., and Han, Q. (2020). Thermodynamic of Collapsing Cavitation Bubble Investigated by Pseudopotential and thermal MRT-LBM. *Ultrason. Sonochem.* 62, 104873. doi:10.1016/j.ultsonch.2019.104873

Yuan, P., and Schaefer, L. (2006). Equations of State in a Lattice Boltzmann Model. *Phys. Fluids* 18, 042101. doi:10.1063/1.2187070

Yusof, N. S. M., Babgi, B., Alghamdi, Y., Aksu, M., Madhavan, J., and Ashokkumar, M. (2016). Physical and Chemical Effects of Acoustic Cavitation in Selected Ultrasonic Cleaning Applications. *Ultrason. Sonochem.* 29, 568–576. doi:10.1016/j.ultsonch.2015.06.013

Zhang, R., and Chen, H. (2003). Lattice Boltzmann Method for Simulations of Liquid-Vapor thermal Flows. *Phys. Rev. E* 67, 066711. doi:10.1103/PhysRevE.67.066711